9. K. J. Maloney *et al.*, *APL Mater.* **1**, 022106 (2013).
10. L. Valdevit, A. Pantano, H. A. Stone, A. G. Evans, *Int. J. Heat Mass Transfer* **49**, 3819–3830 (2006).
11. M. Q. Li, X. Shi, *Rare Metal Mater. Eng.* **36**, 575 (2007).
12. O. Y. Kwon, H. J. Ryu, S. Y. Jeong, *J. Ind. Eng. Chem.* **12**, 306 (2006).
13. R. A. Olson, L. C. B. Martins, *Adv. Eng. Mater.* **7**, 187–192 (2005).
14. P. Day, H. Kind, *Mod. Cast.* **74**, 16 (1984).
15. S. Baudis *et al.*, *Biomed. Mater.* **6**, 055003 (2011).
16. K. Arcaute, B. K. Mann, R. B. Wicker, *Tissue Eng. C* **17**, 27–38 (2010).
17. J. L. Gibson, F. M. Ashby, *Cellular Solids: Structure and Properties* (Cambridge Univ. Press, Cambridge, 2001).
18. H. Fan *et al.*, *Nat. Mater.* **6**, 418–423 (2007).
19. L. Qiu, J. Z. Liu, S. L. Y. Chang, Y. Wu, D. Li, *Nat. Commun.* **3**, 1241 (2012).
20. T. A. Schaedler *et al.*, *Science* **334**, 962–965 (2011).
21. M. A. Worsley, S. O. Kucheyev, J. H. Satcher, A. V. Hamza, T. F. Baumann, *Appl. Phys. Lett.* **94**, 073115 (2009).
22. T. M. Tillotson, L. W. Hrubesh, *J. Non-Cryst. Solids* **145**, 44–50 (1992).
23. S. O. Kucheyev *et al.*, *Adv. Mater.* **24**, 776–780 (2012).
24. L. J. Gibson, *MRS Bull.* **28**, 270–274 (2003).
25. K. Tantikom, Y. Suwa, T. Aizawa, *Mater. Trans.* **45**, 509–515 (2004).
26. A. Torrents, T. A. Schaedler, A. J. Jacobsen, W. B. Carter, L. Valdevit, *Acta Mater.* **60**, 3511–3523 (2012).
27. C. Q. Dam, R. Brezny, D. J. Green, *J. Mater. Res.* **5**, 163–171 (1990).
28. J. K. Cochran, K. J. Lee, D. McDowell, T. Sanders, Multifunctional metallic honeycombs by thermal chemical processing. In *Processsing and Properties of Lightweight Cellular Metals and Structures*, A. K. Ghosh, T. H. Sanders, T. D. Claar, Eds. (Minerals, Metals and Materials Society, Seattle, WA, 2002), p. 127–136.
29. J. Zhang, M. F. Ashby, *Int. J. Mech. Sci.* **34**, 475–489 (1992).
30. D. Rayneau-Kirkhope, Y. Mao, R. Farr, *Phys. Rev. Lett.* **109**, 204301 (2012).
31. K. C. Cheung, N. Gershenfeld, *Science* **341**, 1219–1221 (2013).
32. D. Jang, L. R. Meza, F. Greer, J. R. Greer, *Nat. Mater.* **12**, 893–898 (2013).
33. L. Meza, J. Greer, *J. Mater. Sci.* **49**, 2496–2508 (2014).
34. J. Bauer, S. Hengsbach, I. Tesari, R. Schwaiger, O. Kraft, *Proc. Natl. Acad. Sci. U.S.A.* **111**, 2453–2458 (2014).
35. V. S. Deshpande, N. A. Fleck, M. F. Ashby, *J. Mech. Phys. Solids* **49**, 1747–1769 (2001).
36. J. D. Renton, *Elastic Beams and Frames* (Horwood, Chichester, UK, ed. 2, 2002).
37. S. Hyun, J. E. Choi, K. J. Kang, *Comput. Mater. Sci.* **46**, 73–82 (2009).
38. H. L. Fan, F. N. Jin, D. N. Fang, *Mater. Des.* **30**, 511–517 (2009).
39. See supplementary materials on *Science* Online.
40. W. Y. Jang, S. Kyriakides, A. M. Kraynik, *Int. J. Solids Struct.* **47**, 2872–2883 (2010).
41. Y. Takahashi, D. Okumura, N. Ohno, *Int. J. Mech. Sci.* **52**, 377–385 (2010).
42. X. Zheng *et al.*, *Rev. Sci. Instrum.* **83**, 125001 (2012).
43. C. Sun, N. Fang, D. M. Wu, X. Zhang, *Sens. Actuators A* **121**, 113–120 (2005).
44. A. J. Jacobsen, W. Barvosa-Carter, S. Nutt, *Adv. Mater.* **19**, 3892–3896 (2007).
45. L. M. Moreau *et al.*, *Nano Lett.* **12**, 4530–4539 (2012).

ACKNOWLEDGMENTS

This work was performed under the auspices of the U.S. Department of Energy by Lawrence Livermore National Laboratory under contract DE-AC52-07NA27344. Supported by LDRD Strategic Initiative 11-SI-005 and DARPA MCMA (Materials with Controlled Microstructural Architecture, Program Manager J. Goldwasser). The authors at Lawrence Livermore National Laboratory thank H. Rathbun for useful discussions on modeling the lattice structures, M. Worsley for taking SEM images, and C. Harvey for technical support. N.X.F. thanks S. Cai at University of California San Diego for insightful input regarding buckling modes in ceramic octet-truss lattices (LLNL-JRNL-640334).

SUPPLEMENTARY MATERIALS

www.sciencemag.org/content/344/6190/1373/suppl/DC1
Materials and Methods
Figs. S1 to S9
Table S1
Movies S1 to S3
References (*46*–*55*)

17 February 2014; accepted 16 May 2014
10.1126/science.1252291

NANOMATERIALS

Long-range orientation and atomic attachment of nanocrystals in 2D honeycomb superlattices

M. P. Boneschanscher,[1] W. H. Evers,[2,3] J. J. Geuchies,[1] T. Altantzis,[4] B. Goris,[4] F. T. Rabouw,[1] S. A. P. van Rossum,[1] H. S. J. van der Zant,[3] L. D. A. Siebbeles,[2] G. Van Tendeloo,[4] I. Swart,[1] J. Hilhorst,[5] A. V. Petukhov,[1] S. Bals,[4] D. Vanmaekelbergh[1]*

Oriented attachment of synthetic semiconductor nanocrystals is emerging as a route for obtaining new semiconductors that can have Dirac-type electronic bands such as graphene, but also strong spin-orbit coupling. The two-dimensional (2D) assembly geometry will require both atomic coherence and long-range periodicity of the superlattices. We show how the interfacial self-assembly and oriented attachment of nanocrystals results in 2D metal chalcogenide semiconductors with a honeycomb superlattice. We present an extensive atomic and nanoscale characterization of these systems using direct imaging and wave scattering methods. The honeycomb superlattices are atomically coherent and have an octahedral symmetry that is buckled; the nanocrystals occupy two parallel planes. Considerable necking and large-scale atomic motion occurred during the attachment process.

In oriented attachment, a single nanocrystal (NC) is formed from two adjacent NCs through atomically matched bond formation between two specific facets. Controlled oriented attachment is currently emerging as a route to form extended one- and two-dimensional single-crystalline semiconductors of II-VI and IV-VI compounds (*1*–*5*). These superlattices are of interest in optoelectronics. Truncated nanocubes of the Pb-chalcogenide family (fig. S1) have been recently used to create two-dimensional (2D) atomically coherent ultrathin quantum wells (*4*) as well as superlattices with square or honeycomb geometries (fig. S2) (*5*). The formation of such systems is remarkable, given that several demanding conditions must be fulfilled. The NC building blocks must be nearly monodisperse in size and shape, and attachment should only occur with a geometrically defined subset of NC facets. The long-range atomic and nanoscale order in such systems is far from understood. For extended, atomically coherent PbSe superlattices with honeycomb geometry, immediate questions emerge regarding the large-scale crystallographic orientation of the NCs, the role of surface passivation of specific facets, and the atomic mechanism of attachment.

Here, we report on the atomic and nanoscale analysis of atomically coherent PbSe, PbS, and CdSe honeycomb superlattices. Using high-angle annular dark-field scanning transmission electron microscopy (HAADF-STEM) tomography, we show that the honeycomb structures are buckled—the NCs occupy two parallel planes—and hence show nanoscale analogy with the proposed atomic silicene honeycomb structure. The specific orientation of the NCs in the 2D superlattice extends over hundreds of unit cells, suggesting that such types of single crystals must be formed from a preordered state, for example at the suspension/air interface. Compared with the native building blocks, the NCs in the honeycomb structure are considerably elongated in the direction of the NC-NC bond. This finding points to bond formation via necking accompanied with a gradual release of the capping molecules and considerable atomic motion within the NCs. Moreover, the 2D honeycomb structures of PbSe with a rocksalt atomic lattice were robust enough to be transformed into 2D CdSe lattices with a zinc blende atomic lattice through cation-exchange and keep the nanoscale honeycomb geometry intact. This method opens a route to a new class of 2D semiconductors with tunable composition. In these structures, the nanoscale honeycomb geometry has been predicted to result in both valence and conduction bands that can be filled with Dirac-type charge carriers as in graphene but, unlike graphene, with strong spin-orbit coupling (*6*).

The PbSe NCs have the shape of a cantellated cube, approaching that of a rhombicuboctahedron (fig. S1), implying that the NCs are terminated with {100}, {110}, and {111} facets. We estimated the NC size from the radially averaged diameter of the TEM projections for >1000 particles (5.3 ± 0.4 nm) (fig. S3). The oriented attachment of these NCs resulted in structures with long-range periodicity, as visualized by means of an equilateral triangle spanning the same number of unit cells along each vertex in the HAADF-STEM image (Fig. 1A).

[1]Debye Institute for Nanomaterials Science, University of Utrecht, Post Office Box 80.000, 3508 TA Utrecht, Netherlands. [2]Opto-electronic Materials Section, Delft University of Technology, Julianalaan 136, 2628 BL Delft, Netherlands. [3]Kavli Institute of Nanoscience, Delft University of Technology, Post Office Box 5046, 2600 GA Delft, Netherlands. [4]Electron Microscopy for Materials Science (EMAT), University of Antwerp, Groenenborgerlaan 171, 2020 Antwerp, Belgium. [5]European Synchrotron Radiation Facility (ESRF), Grenoble, Beamline ID01, France.
***Corresponding author. E-mail: d.vanmaekelbergh@uu.nl**

Zooming in on the honeycomb structure (Fig. 1B) reveals that the ⟨111⟩ axes of the NCs are perpendicular to the substrate and that the NC-NC bonds are perpendicular to three of the ⟨110⟩ axes (a discussion on atomic contrast in HAADF-STEM images is available in fig. S4). This result is also corroborated by electron diffraction (ED) patterns (Fig. 1C). The structures have a high degree of crystallinity, as observed with the occurrence of sharp spots in ED patterns recorded on selected areas with a diameter of 200 nm (Fig. 1C; a full analysis of all peaks in the diffraction pattern is available in fig. S5 and tables S1 and S2) (*7*).

There are three different models for attachment of the NCs that result in a honeycomb structure with the nanocrystal ⟨111⟩ axes perpendicular to the substrate: attachments via the {110}, {111}, or {100} facets, respectively (Fig. 1, D to I). The three structures appear similar from the top but have a very different 3D geometry. Attachment via {110} facets results in a planar, trigonal structure with bond angles between the NCs of 120° (Fig. 1, D and E). If the NCs attach via the {111} facets, the overall structure of the superlattice is slightly buckled, with a tetrahedral symmetry and NC bond angles of 109.5° (Fig. 1, F and G). Attachment via {100} facets results in a highly buckled geometry, with an octahedral symmetry and NC bond angles of 90° (Fig. 1, H and I). We used various imaging techniques to show that the experimental structure is of the octahedral type, but that the bond lengths are longer than expected on the basis of a simple block model.

In the trigonal model, the attachment takes place via the {110} facets, meaning that the ⟨110⟩ axes are parallel to the NC bonds. However, both the high-resolution HAADF-STEM images and the ED patterns show that in our experiment, the ⟨110⟩ axes are perpendicular to the NC bonds (Fig. 1, B and C), so we could discard the trigonal model. In the buckling of the honeycomb, the HAADF-STEM images showed additional scattering strength on the NC bonds, indicating a larger-than-average thickness of the sample at that position. In this respect, both the tetrahedral and octahedral model are buckled and have three of the ⟨110⟩ NC axes perpendicular to the NC bonds, so it was impossible to discriminate between these remaining models by ED or 2D projections from high-resolution HAADF-STEM. Thus, we needed to use a combination of scanning tunneling microscopy (STM), grazing-incidence small-angle x-ray scattering

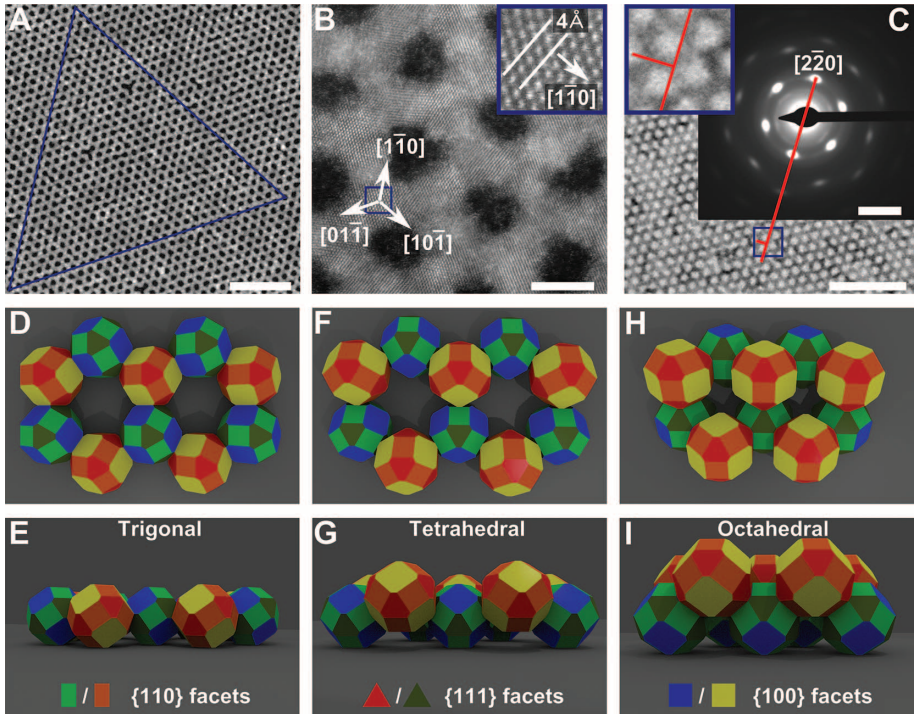

Fig. 1. Single-crystalline PbSe honeycomb structures created by means of oriented attachment. (**A**) HAADF-STEM image of the honeycomb structure (bright on a dark background). The equilateral triangle shows the long-range ordering of the structure. Scale bar, 50 nm. (**B**) High-resolution HAADF-STEM image showing that the ⟨111⟩ NC axes are perpendicular to the honeycomb plane, and three of the ⟨110⟩ axes are perpendicular to the NC bonds. (Inset) Zoom-in on the atomic columns indicated by the blue box. Scale bar, 5 nm. (**C**) Electron diffraction pattern showing the high degree of crystallinity. TEM image in the background shows the area on which the ED pattern was recorded (the honeycomb appears dark on a bright background). Red line and inset show the orientation of the diffraction spots with respect to the honeycomb structure, confirming that the ⟨110⟩ axes are perpendicular to the NC bonds. Scale bars, 50 nm (TEM); 5 nm^{-1} (ED). (**D** to **I**) Models of the honeycomb structure, with cantellated cubes as nanocrystals. The two inequivalent sites in the honeycomb lattice are indicated by yellow/red and blue/green NCs. Rectangles (orange and light green) represent {110} facets, triangles (red and dark green) represent {111} facets, and squares (yellow, blue) represent {100} facets. (D) and (E) are the top and side view of the trigonal structure, respectively. (F) and (G) are top and side view of the tetrahedral structure, respectively. (H) and (I) are the top and side view of the octahedral structure, respectively.

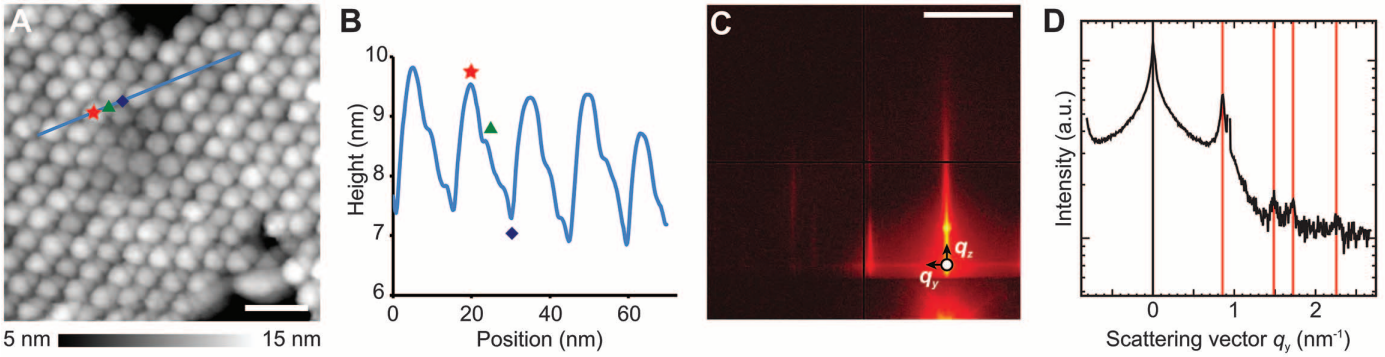

Fig. 2. STM and GISAXS measurements of the PbSe honeycomb structures. (**A**) Constant-current STM measurement showing high (red star) and low (green triangle) nanocrystals forming a honeycomb structure. Feedback settings are 3.5 V and 20 pA. Scale bar, 20 nm. (**B**) Height profile along the blue line indicated in (A). The position of a high NC (star), low NC (triangle), and hollow site (diamond) are indicated. (**C**) GISAXS pattern of a honeycomb structure on top of a Si(100) substrate, under an angle of incidence of 0.7°. Scale bar, 1 nm^{-1}. (**D**) Line trace in the horizontal direction indicated in (C), revealing the in-plane order. Red lines mark diffraction peaks with relative positions of $1:\sqrt{3}:2:\sqrt{7}$, arising from the hexagonal order of the holes in the structure.

(GISAXS), and electron tomography to fully resolve the honeycomb structure.

The STM measurements showed that the honeycomb structure is indeed buckled (Fig. 2, A and B). However, topography in STM is a complicated convolution of NC height and tip radius (fig. S6), so no quantitative height data could be extracted. We cannot measure bond lengths and angles directly in STM, but we could reliably determine the distance between next-nearest neighbors (NNNs) at the same height (8.5 ± 0.8 nm, for >500 measurements). From GISAXS (Fig. 2, C and D, and fig. S7), we observed scattering peaks arising from the hexagonal order of the holes in the honeycomb structure with relative positions of $1:\sqrt{3}:2:\sqrt{7}$, as expected from a honeycomb structure (Fig. 2, C and D). Looking at the absolute peak positions in Fig. 2D, we found a hole-hole distance of 8.5 nm, which is in accordance with the NNN distances observed in STM. Assuming perfect honeycomb models, this distance implies a bond length of 5.2 nm for the tetrahedral and 6.0 nm for the octahedral honeycomb structure.

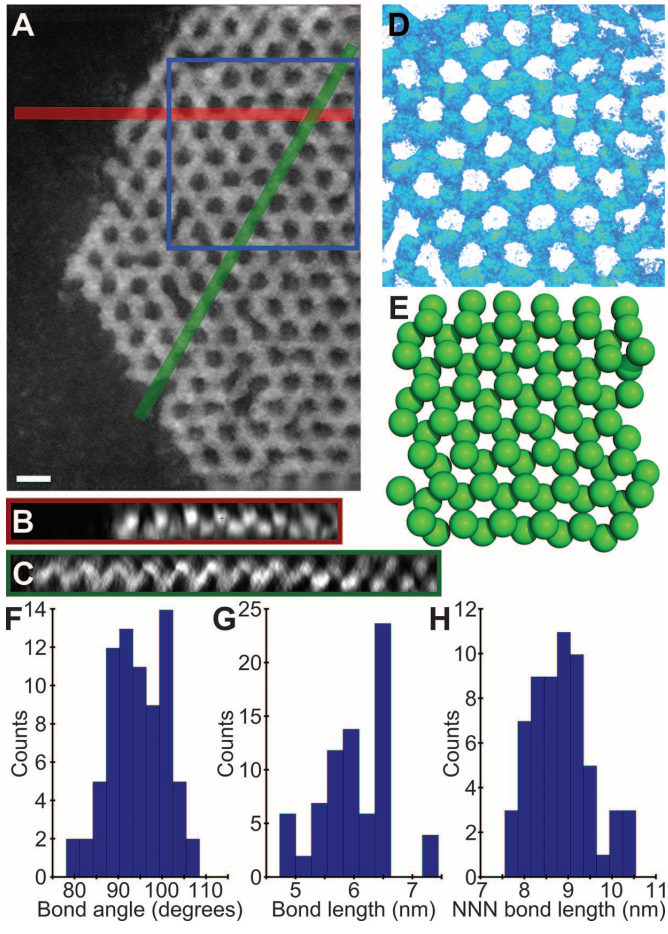

Fig. 3. HAADF-STEM tomography on a PbSe honeycomb structure. (**A**) Overview of the honeycomb structure obtained by averaging the tomographic reconstruction in the direction perpendicular to the substrate. Scale bar, 10 nm. (**B** and **C**) Slices through the tomogram perpendicular to (A), along the (B) red or (C) green line indicated in (A). (**D**) Isovolume rendering of the tomographic reconstruction in the region indicated with the blue box in (A). (**E**) Equally sized spheres plotted on the coordinates obtained by means of automated particle detection in the region indicated in blue in (A). (**F**) Bond angles measured from the coordinates in (E), showing a bond angle of 95 ± 5°. (**G**) Bond lengths to nearest neighbors, showing a bond length of 6.0 ± 0.5 nm. (**H**) Bond lengths to NNNs, showing a NNN bond length of 8.9 ± 0.6 nm.

The tomographic reconstruction of a PbSe honeycomb structure obtained with electron tomography is shown in Fig. 3 (movie S1) (*7*–*10*). Slices through the reconstruction in the direction perpendicular to the substrate indicate that the two inequivalent NCs in the honeycomb unit cell are located on different heights (Fig. 3, B and C) (*11*). We performed automated particle detection (*7*) on the region of interest indicated in Fig. 3D. We remark that the effect of the missing wedge in our tomography data results in a blurring of the contrast along the *z* direction. In (*7*), we used simulated tomography data to show that the missing wedge in this case does not impede objective particle detection (fig. S8). From the resulting coordinates, we constructed a model resembling the tomographic reconstruction (Fig. 3E). Using a Voronoi method, we could measure important parameters such as bond angle, bond length, and NNN bond length (Fig. 3, F to H).

The obtained bond angle of 95° ± 5° (Fig. 3F) shows that the honeycomb structure is of the octahedral type, with bonds between the {100} facets. We can compare the ratio between bond length (6.0 ± 0.5 nm) and NNN bond length (8.9 ± 0.6 nm) that we find with the theoretical values for the different structures—for the octahedral type, one would expect $1:\sqrt{2}$; for the tetrahedral type, $1:\sqrt{8/3}$; and for the trigonal type, $1:\sqrt{3}$. The ratio we find here (1:1.48) is a bit higher than the expected ratio for an octahedral structure, which is in agreement with the bond angles being slightly higher than 90°. The same measurement on a tomogram of a CdSe honeycomb structure shows bond angles of 85° ± 6°, which is slightly lower than expected (figs. S9 and S10 and movie S2).

We established that the NCs attach via the {100} facets into a honeycomb structure with octahedral symmetry (Fig. 1, H and I). Next, we returned to the bond lengths of the honeycomb structure, as extracted from TEM (fig. S11), STM, GISAXS, and tomography. All four techniques give an independent measure of 6.0 nm for the NC bond lengths, which is an increase of 13% of the original NC diameter. The increased bond lengths shed light on the microscopic mechanism of facet-to-facet atomic attachment. Li *et al.* (*12*) showed that in the process of oriented attachment, the NCs are continuously rotating and moving in close proximity by means of Brownian motion to find an optimum configuration before enduring attachment takes place. We propose that during the rotation and Brownian motion as described by Li *et al.* (*12*), atomic-scale necking took place as a first step in the attachment. After necking had started, the capping molecules that remain bound to the facet were gradually removed,

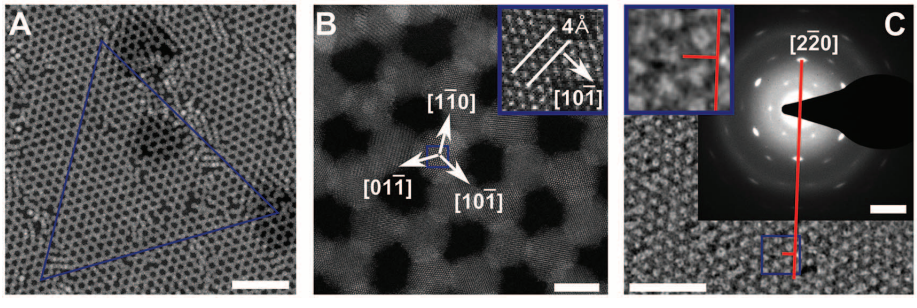

Fig. 4. Single crystalline CdSe honeycomb structures created by cation exchange. (**A**) HAADF-STEM image of the CdSe honeycomb structure. The honeycomb appears bright on a dark background. The equilateral triangle shows that the long-range ordering of the structure is retained. Scale bar, 50 nm. (**B**) High-resolution HAADF-STEM image showing that the orientation of the Se anion lattice with respect to the superlattice geometry is preserved. (Inset) Zoom-in on the area indicated by the blue box. Scale bar, 5 nm. (**C**) An ED pattern showing that the high degree of crystallinity is preserved. TEM image in the background shows the area on which the ED pattern was recorded (the honeycomb appears dark on a bright background). Red line and inset show the orientation of the diffraction spots with respect to honeycomb structure, confirming that the ⟨110⟩ axes are perpendicular to the NC bonds. Scale bars, 50 nm (TEM); 5 nm^{-1} (ED).

and the neck extended perpendicular to the bond axis through large-scale atomic motion. For PbSe NCs, considerable atomic reconfigurations have been reported (*13*, *14*). The necking explains the elongation of the bond lengths, which also results in a considerably more open honeycomb structure than can be obtained from geometric attachment of rigid block models (Fig. 1H, as compared with the real structures in Figs. 1, A to C, 3, and 4). In the mechanism that we propose, not all of the capping molecules have to be released at once from a facet, resulting in pathways with lower activation energy. Oriented attachment accompanied with neck formation has been reported before as a pathway for the growth of various metal nanoparticles (*15*, *16*).

Since the emergence of graphene (*17*), there has been a general interest in the properties of electrons confined in a honeycomb lattice (*18*–*23*). We show that oriented attachment can form the basis of a generally applicable two-step method for the preparation of 2D semiconductors with nanoscale honeycomb geometry: assembly and oriented attachment of Pb-chalcogenide NCs with truncated cubic shape, followed by cation exchange. It has been predicted that honeycomb semiconductors of zinc blende compounds (such as CdSe) show a truly new electronic band structure, with a valence hole Dirac band and one or two conduction electron Dirac bands combined with strong spin-orbit coupling (*6*). We transformed PbSe honeycomb structures into CdSe superlattices via a cation exchange reaction (*24*, *25*) and showed that honeycomb structures can also be prepared from PbS NCs (figs. S12 and S13).

The successful exchange of a PbSe honeycomb lattice into a CdSe honeycomb is presented in Fig. 4. The complete transformation of the PbSe lattice into CdSe is confirmed by means of energy-dispersive x-ray spectroscopy (fig. S14). HAADF-STEM and ED measurements show that the orientation of the Se anion lattice with respect to the honeycomb periodicity is preserved (Fig. 4, A to C). This result is in agreement with earlier described mechanisms in which the anion lattice is preserved during cation exchange (*26*, *27*) and is corroborated with high-resolution HAADF-STEM measurements of honeycomb structures at intermediate stages of cation exchange (*7*).

REFERENCES AND NOTES

1. C. Pacholski, A. Kornowski, H. Weller, *Angew. Chem. Int. Ed. Engl.* **41**, 1188–1191 (2002).
2. K.-S. Cho, D. V. Talapin, W. Gaschler, C. B. Murray, *J. Am. Chem. Soc.* **127**, 7140–7147 (2005).
3. W. K. Koh, A. C. Bartnik, F. W. Wise, C. B. Murray, *J. Am. Chem. Soc.* **132**, 3909–3913 (2010).
4. C. Schliehe *et al.*, *Science* **329**, 550–553 (2010).
5. W. H. Evers *et al.*, *Nano Lett.* **13**, 2317–2323 (2013).
6. E. Kalesaki *et al.*, *Phys. Rev. X* **4**, 011010 (2014).
7. Materials and methods are available as supplementary materials on *Science* Online.
8. H. Friedrich *et al.*, *Nano Lett.* **9**, 2719–2724 (2009).
9. M. P. Boneschanscher *et al.*, *Nano Lett.* **13**, 1312–1316 (2013).
10. P. A. Midgley, M. Weyland, *Ultramicroscopy* **96**, 413–431 (2003).
11. The PbSe honeycombs suffer from beam damage, making it hard to obtain high-quality tomographic reconstructions. CdSe, on the other hand, is more stable under the electron beam, resulting in higher-quality tomographic reconstructions (Fig. 3 as compared with fig. S9, for example. Both images are obtained under the same conditions).
12. D. Li *et al.*, *Science* **336**, 1014–1018 (2012).
13. M. A. van Huis *et al.*, *Nano Lett.* **8**, 3959–3963 (2008).
14. M. A. van Huis *et al.*, *Adv. Mater.* **21**, 4992–4995 (2009).
15. J. M. Yuk *et al.*, *Science* **336**, 61–64 (2012).
16. J. M. Yuk *et al.*, *Chem. Commun. (Camb.)* **49**, 11479–11481 (2013).
17. A. H. Castro Neto, N. M. R. Peres, K. S. Novoselov, A. K. Geim, *Rev. Mod. Phys.* **81**, 109–162 (2009).
18. K. K. Gomes, W. Mar, W. Ko, F. Guinea, H. C. Manoharan, *Nature* **483**, 306–310 (2012).
19. G. De Simoni *et al.*, *Appl. Phys. Lett.* **97**, 132113 (2010).
20. M. Gibertini *et al.*, *Phys. Rev. B* **79**, 241406 (2009).
21. C.-H. Park, S. G. Louie, *Nano Lett.* **9**, 1793–1797 (2009).
22. C.-H. Park, L. Yang, Y.-W. Son, M. L. Cohen, S. G. Louie, *Phys. Rev. Lett.* **101**, 126804 (2008).
23. A. Singha *et al.*, *Science* **332**, 1176–1179 (2011).
24. J. M. Luther, H. Zheng, B. Sadtler, A. P. Alivisatos, *J. Am. Chem. Soc.* **131**, 16851–16857 (2009).
25. B. J. Beberwyck, Y. Surendranath, A. P. Alivisatos, *J. Phys. Chem. C* **117**, 19759–19770 (2013).
26. S. Bals *et al.*, *Nano Lett.* **11**, 3420–3424 (2011).
27. M. Casavola *et al.*, *Chem. Mater.* **24**, 294–302 (2012).

ACKNOWLEDGMENTS

We thank ESRF (Grenoble, France) for providing the synchrotron beamtime and the staff of ESRF beamline ID-01 for their support. We thank C. van Overbeek for his help on the PbS sample. This research is part of the programs "Control over Functional Nanoparticle Solids (FNS)" and "Designing Dirac Carriers in semiconductor honeycomb superlattices (DDC)," which are supported by the Foundation of Fundamental Research on Matter (FOM), which is part of the Dutch Research Council (NWO). The authors also acknowledge financial support from the European Research Council (ERC Advanced Grant 24691-COUNTATOMS and ERC Starting Grant #335078-COLOURATOM). The authors also appreciate financial support from the European Union under the Seventh Framework Program [Integrated Infrastructure Initiative 262348 European Soft Matter Infrastructure (ESMI)]. This work was supported by the Flemish Fund for Scientific Research (FWO Vlaanderen) through a Ph.D. research grant to B.G.

SUPPLEMENTARY MATERIALS

www.sciencemag.org/content/344/6190/1377/suppl/DC1
Materials and Methods
Figs. S1 to S14
Tables S1 to S2
References (*28*, *29*)
Movies S1 to S2

25 February 2014; accepted 13 May 2014
Published online 29 May 2014;
10.1126/science.1252642

NANOMATERIALS

Hydroxylation of the surface of PbS nanocrystals passivated with oleic acid

Danylo Zherebetskyy,[1] Marcus Scheele,[1,2] Yingjie Zhang,[1,3] Noah Bronstein,[2] Christopher Thompson,[1,2] David Britt,[4] Miquel Salmeron,[1] Paul Alivisatos,[1,2] Lin-Wang Wang[1]*

Controlling the structure of colloidal nanocrystals (NCs) is key to the generation of their complex functionality. This requires an understanding of the NC surface at the atomic level. The structure of colloidal PbS NCs passivated with oleic acid has been studied theoretically and experimentally. We show the existence of surface OH^- groups, which play a key role in stabilizing the PbS(111) facets, consistent with x-ray photoelectron spectroscopy as well as other spectroscopic and chemical experiments. The role of water in the synthesis process is also revealed. Our model, along with existing observations of NC surface termination and passivation by ligands, helps to explain and predict the properties of NCs and their assemblies.

The structure of the interior of nanocrystals (NCs) can be determined quite accurately by crystallography, but the structure of their surfaces cannot be obtained from this analysis because of the complexity of the organic capping ligands (*1*–*6*). However, the NC surface structure controls the growth and solubility and strongly influences the physical and chemical properties (*7*–*12*). We took advantage of improved insights into the mechanisms of NC growth (*3*–*6*), combined with extensive ab initio total energy calculations, to create a testable model for the atomic surface passivation structure of the exposed facets of a PbS NC. The model made specific, and at first surprising, predictions about the surface-bound species that were subsequently verified experimentally. PbS is ideal for this study because of the high symmetry of its rock-salt structure and its propensity to form NCs with well-defined (111) and (001) facets (*13*, *14*). PbS NCs with controlled size and shape can be produced from a PbO lead precursor, hexamethyldisilathiane (TMS_2S) sulfur precursor, and oleic acid that binds to exposed Pb atoms to stabilize the surface (*1*–*6*).

We performed ab initio electronic structure calculations on relevant subsystems and on the reaction steps involved in the synthetic process, including studies of immediate precursors, the fate of byproducts of the initial decomposition step, NC-ligand interactions, and ligand-ligand and ligand-solvent

[1]Materials Sciences Division, Lawrence Berkeley National Laboratory, Berkeley, CA 94720, USA. [2]Department of Chemistry, University of California at Berkeley, Berkeley, CA 94720, USA. [3]Applied Science and Technology Graduate Program, University of California at Berkeley, Berkeley, CA 94720, USA. [4]The Molecular Foundry, Lawrence Berkeley National Laboratory, One Cyclotron Road, Berkeley, CA 94720, USA.
***Corresponding author. E-mail: lwwang@lbl.gov**

Long-range orientation and atomic attachment of nanocrystals in 2D honeycomb superlattices

M. P. Boneschanscher, W. H. Evers, J. J. Geuchies, T. Altantzis, B. Goris, F. T. Rabouw, S. A. P. van Rossum, H. S. J. van der Zant, L. D. A. Siebbeles, G. Van Tendeloo, I. Swart, J. Hilhorst, A. V. Petukhov, S. Bals and D. Vanmaekelbergh (May 29, 2014)

Science **344** (6190), 1377-1380. [doi: 10.1126/science.1252642] originally published online May 29, 2014

Editor's Summary

Nanoparticle lattices and surfaces

The challenge of resolving the details of the surfaces or assemblies of colloidal semiconductor nanoparticles can be overcome if several characterization methods are used (see the Perspective by Boles and Talapin). Boneschanscher *et al.* examined honeycomb superlattices of lead selenide nanocrystals formed by the bonding of crystal faces using several methods, including high-resolution electron microscopy and tomography. The structure had octahedral symmetry with the nanocrystals distorted through "necking": the expansion of the contact points between the nanocrystals. Zherebetskyy *et al.* used a combination of theoretical calculations and spectroscopic methods to study the surface layer of lead sulfide nanocrystals synthesized in water. In addition to the oleic acid groups that capped the nanocrystals, hydroxyl groups were present as well.

Science, this issue p. 1377, p. 1380; see also p. 1340

Science (print ISSN 0036-8075; online ISSN 1095-9203) is published weekly, except the last week in December, by the American Association for the Advancement of Science, 1200 New York Avenue NW, Washington, DC 20005.